Analysis of the Precision of Variable Flip Angle T_1 Mapping with Emphasis on the Noise Propagated from RF Transmit Field Maps

Yoojin Lee [1,2]*, Martina F. Callaghan [3] and Zoltan Nagy [1,2]

[1] Laboratory for Social and Neural Systems Research, University of Zürich, Zürich, Switzerland, [2] Department of Information Technology and Electrical Engineering, Institute of Biomedical Engineering, ETH Zürich, Zürich, Switzerland, [3] Wellcome Trust Centre for Neuroimaging, UCL Institute of Neurology, University College London, London, UK

In magnetic resonance imaging, precise measurements of longitudinal relaxation time (T_1) is crucial to acquire useful information that is applicable to numerous clinical and neuroscience applications. In this work, we investigated the precision of T_1 relaxation time as measured using the variable flip angle method with emphasis on the noise propagated from radiofrequency transmit field (B_1^+) measurements. The analytical solution for T_1 precision was derived by standard error propagation methods incorporating the noise from the three input sources: two spoiled gradient echo (SPGR) images and a B_1^+ map. Repeated *in vivo* experiments were performed to estimate the total variance in T_1 maps and we compared these experimentally obtained values with the theoretical predictions to validate the established theoretical framework. Both the analytical and experimental results showed that variance in the B_1^+ map propagated comparable noise levels into the T_1 maps as either of the two SPGR images. Improving precision of the B_1^+ measurements significantly reduced the variance in the estimated T_1 map. The variance estimated from the repeatedly measured *in vivo* T_1 maps agreed well with the theoretically-calculated variance in T_1 estimates, thus validating the analytical framework for realistic *in vivo* experiments. We concluded that for T_1 mapping experiments, the error propagated from the B_1^+ map must be considered. Optimizing the SPGR signals while neglecting to improve the precision of the B_1^+ map may result in grossly overestimating the precision of the estimated T_1 values.

Keywords: B_1^+ map, T_1 map, error propagation, uncertainty, precision, variable flip angle

INTRODUCTION

Measurement of the longitudinal relaxation time (T_1) of a sample is of paramount importance as evidenced by the fact that methods for its measurement appeared soon after the invention of NMR (Drain, 1949; Hahn, 1949). In MRI T_1 mapping is widely used because it provides insight into the microstructure of brain tissue (Harkins et al., 2016) and can act as a biomarker of myelination (Dick et al., 2012; Lutti et al., 2013; Sereno et al., 2013). Hence, numerous T_1 mapping methods are available (Kingsley, 1999). Although, typically taken as the gold standard, the inversion recovery approach is very time consuming (Stikov et al., 2015). Instead, the combination of multiple three

dimensional (3D) spoiled gradient echo (SPGR) (Haase et al., 1986) images with short repetition times, variable flip angles (VFA) (Christensen et al., 1974; Fram et al., 1987) and appropriate spoiling (Zur et al., 1991; Ganter, 2006) offers a means of obtaining whole brain T_1 maps in clinically feasible times (Deoni et al., 2005; Helms et al., 2008).

Several factors affect the accuracy and/or precision of T_1 measurements obtained via the VFA method (Wang et al., 1987; Deoni et al., 2004; Preibisch and Deichmann, 2009; Schabel and Morrell, 2009; Helms et al., 2011; Wood, 2015). In particular, the bias introduced by the spatial inhomogeneity of the radiofrequency (RF) transmit field (B_1^+) is a well-known source of error (Stikov et al., 2015). Numerous methods exist for obtaining a B_1^+ map (Insko and Bolinger, 1993; Cunningham et al., 2006; Jiru and Klose, 2006; Dowell and Tofts, 2007; Yarnykh, 2007; Lutti et al., 2010; Sacolick et al., 2010; Nehrke and Börnert, 2012) and incorporating this into the T_1 mapping pipeline has been shown to improve the accuracy of the estimated value of the T_1 relaxation times (Venkatesan et al., 1998; Deoni, 2007; Helms et al., 2008; Lutti et al., 2013; Liberman et al., 2014). However, the precision of the B_1^+ map and how this diminishes the precision of the estimated T_1 values has not been thoroughly addressed, especially not *in vivo*. Recently, a systematic comparison of the precision of different B_1^+ mapping methods was performed by Pohmann and Scheffler (2013). They reported the uncertainty in the measurements of the B_1^+ maps and found that the error could be up to approximately 30% for 3D variants. The results of their simulations and phantom experiments agreed well, but they did not investigate the precision of the B_1^+ mapping methods *in vivo* (expected to produce higher uncertainty) nor its impact on the estimated T_1 relaxation times.

To further understand and quantify the effect of uncertainty (i.e., random variability) in B_1^+ maps on the precision of T_1 mapping, a theoretical framework that can be applied *in vivo* and that considers the measurement uncertainty not only in the SPGR signals but also in the B_1^+ maps is needed. Hence the aims of this paper are:

a) To theoretically investigate, within the clinically-feasible VFA approach, the propagation of noise from B_1^+ measurements to the estimated T_1 values and compare this to the error propagated from the SPGR data.
b) To verify that these theoretical estimates are valid for *in vivo* neuroimaging experiments.
c) To show that decreasing the variability in B_1^+ measurements can dramatically increase the precision of estimated T_1 values.

MATERIALS AND METHODS

Theory

Before proceeding with the theoretical framework for analyzing T_1 precision, two terms, accuracy and precision, have to be defined clearly. Accuracy represents how close, on average, the measured value is to the true value and is often dependent on the level of systematic error present in the measurement. The deviation of the average measured value from the true value due to the systematic error is termed bias. On the other hand, precision represents how close the values from the repeated measurements are to each other and will depend on multiple factors, e.g., the sensitivity of the measurement device. Thus, the precision is a measure of uncertainty in the measurement irrespective of the true value. **Figure 1A** shows examples of measurements that are both accurate and precise, which is the target measurement scenario. Measurements can also be accurate but imprecise (**Figure 1B**), inaccurate but precise (**Figure 1C**), and neither accurate nor precise (**Figure 1D**). To collect a single data point with the hope that it is close to the true value, both accuracy and precision are important.

If the transverse magnetization is adequately spoiled before each RF pulse the SPGR signal amplitude is a function of T_1, equilibrium magnetization (M_0), effective transverse relaxation time (T_2^*), and imaging parameters, i.e., the repetition time (TR), flip angle α and echo time (TE) (Fram et al., 1987)

$$S = A\sin(\alpha)\frac{1 - exp(-\text{TR}/T_1)}{1 - cos(\alpha) \cdot exp(-\text{TR}/T_1)} \quad (1)$$

where $A = S_0 exp(-\text{TE}/T_2^*)$. Here S_0 is defined as M_0 multiplied by the receive gain of the system and the receive coil sensitivity. Recently, rational approximation of the SPGR signal for small flip angles and short TR was suggested, which provides a simpler form of Equation (1) (Helms et al., 2008),

$$S \cong A\alpha\frac{\text{TR}/T_1}{\alpha^2/2 + \text{TR}/T_1} \quad (2)$$

By acquiring two SPGR signals, S_1 and S_2, at two different flip angles, α_1 and α_2, T_1 estimates can be obtained with a simple algebraic expression (Helms et al., 2008),

$$T_1 = 2\text{TR}\frac{S_1/\alpha_1 - S_2/\alpha_2}{S_2\alpha_2 - S_1\alpha_1} \quad (3)$$
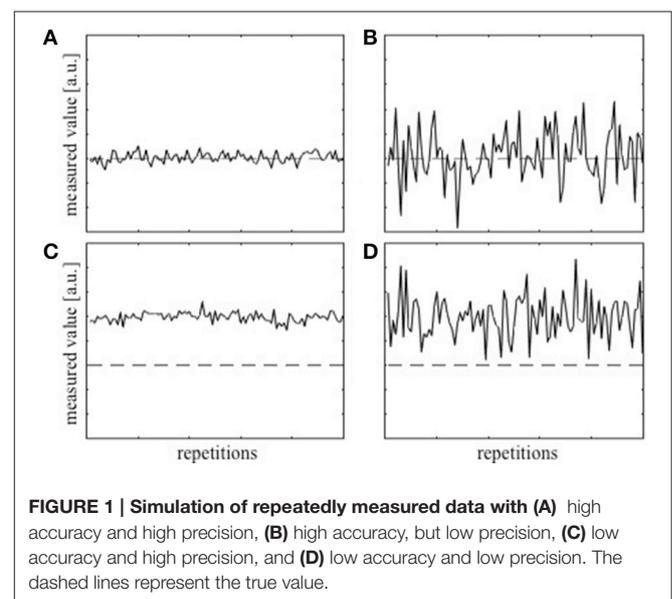
FIGURE 1 | Simulation of repeatedly measured data with (A) high accuracy and high precision, **(B)** high accuracy, but low precision, **(C)** low accuracy and high precision, and **(D)** low accuracy and low precision. The dashed lines represent the true value.

Since the VFA method relies on the flip angle dependency of the SPGR signal for T_1 estimation, a correction for B_1^+ inhomogeneities is necessary in order to obtain unbiased T_1 estimates. The spatially dependent B_1^+ correction factor, denoted as f_{B1}, can be determined by normalizing the B_1^+ map such that 1 is the nominal flip angle. By multiplying α_1 and α_2 by f_{B1} in Equation (3) the B_1^+ bias corrected T_1 equation can be obtained (Helms et al., 2008),

$$T_1 = 2\mathrm{TR}\frac{S_1/\alpha_1 - S_2/\alpha_2}{S_2\alpha_2 - S_1\alpha_1}\frac{1}{f_{B1}^2} \qquad (4)$$

Measurement of a B_1^+ map and inclusion of the correction factor, f_{B1}, in Equation [4] is intended to ensure the accuracy of the T_1 estimates (Stikov et al., 2015). This correction is assumed to correspond to going from **Figure 1C** to **Figure 1A**. However, unless the precision of the B_1^+ map is high, the actual correction may correspond to going from **Figure 1D** to **Figure 1B**, or worse going from **Figure 1C** to **Figure 1B** thereby lowering the precision of the T_1 estimate.

In the general VFA case, an expression for the variance of the estimated T_1 ($\sigma_{T_1}^2$) can be calculated for a set of SPGR signals (S_1, S_2, …, and S_N) measured with N different flip angles and a B_1^+ map (f_{B1}) (Bevington and Robinson, 2003). Assuming statistically independent measurements of each signal the variance in the T_1 estimate is

$$\sigma_{T_1}^2 = \sum_{i=1}^{N}\left(\sigma_{S_i}^2\left(\frac{\partial T_1}{\partial S_i}\right)^2\right) + \sigma_{f_{B1}}^2\left(\frac{\partial T_1}{\partial f_{B1}}\right)^2 \qquad (5)$$

where σ_{S_i} and $\sigma_{f_{B1}}$ are the noise levels in S_i and f_{B1} respectively. For the VFA T_1 mapping technique proposed by Helms et al. (2008) only two SPGR signals are acquired ($N = 2$) and T_1 is calculated from Equation (4). Hence the variance of the estimated T_1 propagated from a B_1^+ map expressed by the second term in Equation (5) is determined by the noise in a B_1^+ map ($\sigma_{f_{B1}}$) and the partial derivative term which can be obtained from Equation (4):

$$\frac{\partial T_1}{\partial f_{B1}} = \frac{4\mathrm{TR}}{f_{B1}^3}\cdot\frac{S_2\alpha_1 - S_1\alpha_2}{a_1\alpha_2\,(S_2\alpha_2 - S_1\alpha_1)} \qquad (6)$$

The T_1 variance propagated from the two SPGR signals can be determined in the same way by the partial derivative terms with respect to S_i:

$$\frac{\partial T_1}{\partial S_1} = \frac{2\mathrm{TR}}{f_{B1}^2}\cdot\frac{S_2\left(\alpha_2^2 - \alpha_1^2\right)}{\alpha_1\alpha_2(S_2\alpha_2 - S_1\alpha_1)^2} \qquad (7)$$

$$\frac{\partial T_1}{\partial S_2} = \frac{2\mathrm{TR}}{f_{B1}^2}\cdot\frac{-S_1\left(\alpha_2^2 - \alpha_1^2\right)}{\alpha_1\alpha_2(S_2\alpha_2 - S_1\alpha_1)^2} \qquad (8)$$

Each partial derivative term in Equations (6–8) is a weighting factor for the noise in the corresponding input signal (i.e., S_1, S_2, and f_{B1}) in Equation (5).

MR Data Collection

Data were collected on four adult volunteers using a 3T MRI scanner (Achieva Platform, Philips Healthcare, Best, The Netherlands). Four different experiments were performed. The first two experiments involved all four volunteers and the input variable f_{B1} was repeatedly measured either with small (**Experiment 1**) or with large spoiler gradients (**Experiment 2**) to assess two different levels of variance in the B_1^+ measurements. On one of the volunteers, the other two input variables, S_1 and S_2, were also repeatedly measured (**Experiments 3** and **4** respectively) to assess their variances and compare them with the variance introduced by the B_1^+ measurements.

Before each measurement the scanner performed a full preparatory phase of shimming, center frequency determination and RF transmit power calibration. The repeated measurements approach adopted here captured all noise sources, e.g., thermal/physiological noise, scanner stability, etc. In summary, the four different experiments were designed as follows:

> **Experiment 1:** one S_1, one S_2, and six B_1^+ maps with small spoiler gradients.
> **Experiment 2:** one S_1, one S_2, and six B_1^+ maps with large spoiler gradients.
> **Experiment 3:** six S_1, one S_2, and one B_1^+ map with large spoiler gradients.
> **Experiment 4:** one S_1, six S_2, and one B_1^+ map with large spoiler gradients.

The 3D SPGR sequence had 0.8 mm isotropic voxels, TR/TE1/TE2/TE3 = 25.0/4.6/11.5/18.3 ms, sensitivity encoding (SENSE) (Pruessmann et al., 1999) factor = 2.0, and scan time = 11.6 min. The SPGR images acquired at three different echo times were averaged to increase the signal-to-noise ratio (SNR) (Helms et al., 2008). The S_1 and S_2 images were acquired with the nominal flip angles of $\alpha_1 = 6°$ and $\alpha_2 = 20°$ respectively, resulting in images with predominantly proton-density (PD) weighting or T_1 weighting. The B_1^+ maps were acquired at 4.0 mm isotropic resolution using the actual flip angle imaging (AFI) method (Yarnykh, 2007) with either small (A_{G1}/A_{G2}=45.33/761.2 mT.ms/m and TR1/TR2/TE = 20/100/2.2 ms) or large (A_{G1}/A_{G2}=931.8/1971.0 mT.ms/m, TR1/TR2/TE = 46/138/2.2 ms) spoiler gradients. A_{G1} and A_{G2} are the spoiler gradient areas on one axis for the interleaved acquisitions with TR1 and TR2, respectively. A nominal flip angle of 60° was used for this AFI B_1^+ map. To match the scan time (5.2 min) of the AFI acquisitions, the protocol using large spoilers also used a SENSE factor of 1.7. The six repetitions were chosen with consideration of the subject's ability to stay still during the measurements. To ascertain that six repetitions were adequate for a reliable estimate of the variability of input signals, variance was also calculated from the first three, first four and first five repetitions separately. The variance distribution converged after five measurements indicating that the estimate was stable and valid (data not shown).
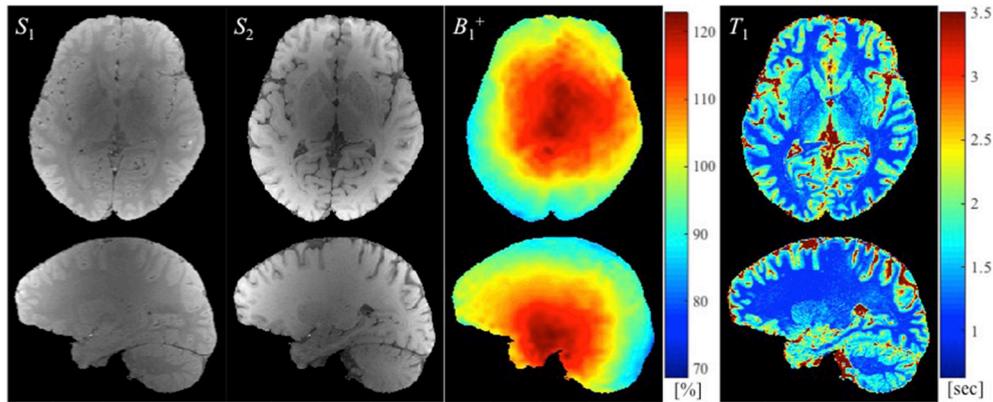
FIGURE 2 | The SPGR images with two different flip angles (S_1 and S_2 in arbitrary units), the B_1^+ map (in the percentage of nominal flip angle), and the estimated T_1 map (in seconds) are shown from left to right.

Data Analysis

All images (S_1, S_2, and the B_1^+ map) were aligned to the first PD weighted image (i.e., the first of the six S_1 in **Experiment 3**) using rigid body registration as implemented in SPM8 (Wellcome Trust Centre for Neuroimaging, UCL, UK). The B_1^+ maps were aligned by using the transformation matrix obtained in the alignment of the corresponding short TR AFI image to the first PD weighted image. Data were evaluated in two different ways to compare the T_1 variances estimated from the *in vivo* measurements and the theoretical framework:

Experimental variance evaluation: Using Equation (4) six T_1 maps were calculated for each of **Experiments 1–4**. The voxel-wise variance across these six T_1 maps was then calculated. With this approach, the experimental noise level in the T_1 map, $\sigma_{T_1,\mathrm{exp}}$, was obtained.

Theoretical variance evaluation: The voxel-wise variance of the repeated S_1, S_2, or B_1^+ scans (i.e., $\sigma_{S_1}^2$, $\sigma_{S_2}^2$, or σ_{fB1}^2) was calculated and inserted into the theoretical noise propagation framework [Equations (5–8)], while assuming zero variance for the other two input signals. For example, in **Experiment 1** we assumed $\sigma_{S_1}^2 = \sigma_{S_2}^2 = 0$ and evaluated $\sigma_{T_1}^2$ by multiplying σ_{fB1}^2 (obtained from the repeated *in vivo* experiments) by the square of the expression given in Equation (6). $\sigma_{T_1}^2$ was similarly evaluated for **Experiments 2–4**. σ_{T_1} calculated by this approach is the theoretically-predicted voxel-wise noise level in the T_1 map and is denoted by $\sigma_{T_1,\mathrm{theo}}$.

Subsequently, coefficient of variation ($CV = 100 \times$ standard deviation / mean) maps were calculated to ease comparison of results across **Experiments 1–4**. Note that CV is inversely proportional to SNR.

The PD weighted image (S_1) was segmented using SPM8 to extract the gray matter (GM) and white matter (WM) segments, which were subsequently thresholded at 0.9 (i.e., 90% probability of belonging to the respective tissue types). The resulting GM and WM masks were used to extract voxel-wise values from the three input images, the T_1 maps and the corresponding CV maps. The median and interquartile range (IQR) of the CV values were then calculated for each tissue type independently.

RESULTS

Example images used to calculate T_1 maps in the work described here, namely two SPGR images (S_1 and S_2) and a B_1^+ map (in this case with large spoiler gradients) are shown in **Figure 2** along with the resulting T_1 map.

Figure 3 provides the results of both methods of variance estimation for **Experiments 1–2**. Column 1 shows the CV maps calculated from the variance across the repeated B_1^+ measurements, i.e., σ_{fB1}^2, with small (**Figure 3a**) and large (**Figure 3e**) spoiler gradients. The experimental and theoretical evaluations of the noise level in the T_1 map propagated from the variance in the B_1^+ map (i.e., $\sigma_{T_1,\mathrm{exp}}$ and $\sigma_{T_1,\mathrm{theo}}$) are shown in column 2 and 3 respectively. Increased spoiling resulted in improved precision of the B_1^+ maps (compare **Figure 3a** with **Figure 3e**), which in turn reduced the variance of the T_1 estimates both experimentally and theoretically (compare **Figure 3b** with **Figure 3f** and **Figure 3c** with **Figure 3g**). Column 4 shows the percentage difference map between the experimentally-measured ($\sigma_{T_1,\mathrm{exp}}$) and the theoretically-predicted ($\sigma_{T_1,\,\mathrm{theo}}$) noise levels in T_1. In general the discrepancy between $\sigma_{T_1,\mathrm{exp}}$ and $\sigma_{T_1,\,\mathrm{theo}}$ was small. For **Experiment 1** (small spoiler), the mean discrepancies (average of absolute percentage difference values) were 1.97 and 1.44% in GM and WM respectively. For **Experiment 2** (large spoiler) these mean discrepancies were reduced to 0.52 and 0.46% respectively. The discrepancy maps (**Figures 3a,h**) show that, if the noise in the input signal is small, the theoretical prediction works better. This is expected from Equation (5).

Figure 4 shows the results of **Experiments 3** and **4** where S_1 and S_2 were measured repeatedly as a comparison to the repeated acquisitions of the B_1^+ maps. **Figure 4a,e** show the CV maps across the repeated measurements of S_1 and S_2 (i.e., *PD*-weighted and T_1-weighted signal respectively). The results of **Experimental and Theoretical variance evaluations** and

FIGURE 3 | CV maps of (a,e) the six f_{B1} acquired with small and large spoiler gradients in **Experiments 1** and **2, (b,f)** the noise of the measured T_1 maps (**Experimental variance evaluation**), and **(c,g)** the theoretically-predicted noise in the T_1 map from the second term in Equation (5), i.e., $100 \cdot \sigma_{f_{B1}} \cdot (\partial T_1/\partial f_{B1})/\hat{T}_1$ (**Theoretical variance evaluation**). **(d,h)** The percentage difference maps between experimentally-measured and theoretically-predicted noise in T_1 estimates. All CV maps shown were calculated by the equations shown in the corresponding gray boxes multiplied by 100. Here, $\hat{f}_{B1}$ and $\hat{T}_1$ represent the means across six f_{B1} and corresponding T_1 maps respectively.

the percentage difference map between them are shown in **Figures 4b–d,f–h** respectively. The mean discrepancies between $\sigma_{T_1,\,\mathrm{exp}}$ and $\sigma_{T_1,\mathrm{theo}}$ in GM/WM were 0.62/0.37% and 3.03/1.73% for **Experiments 3** and **4** respectively. The larger discrepancy between theory and experiment in **Experiment 4** (**Figure 4h**) compared to **Experiment 3** (**Figure 4d**) could be attributed to the larger input noise in the repeated S_2 measurements (**Figure 4e**) than in the repeated S_1 measurements (**Figure 4a**). Nonetheless, the fact that the overall discrepancies are small (column 4 of **Figures 3**, **4**) demonstrates the validity of the theoretical framework presented in Equations (5–8) for estimating the variance in T_1 maps measured *in vivo*.

Histograms of the CV maps for GM and WM are shown in **Figure 5** from the voxel-wise variance in the input images (solid lines), CV maps obtained with **Experimental variance evaluation** (dashed lines) or **Theoretical variance evaluation**

(circles) for **Experiments 1–4**. The histogram of the theoretically-predicted CV values agreed well with that of the experimentally-calculated CV values. Note that the histograms for **Experiment 2** (cyan) shifted toward lower CV values and sharpened significantly compared to those for **Experiment 1** (red), indicating that the T_1 precision was greatly improved by the increased spoiler gradients, across the entire brain. Except for the distributions from **Experiment 1** with small spoiler gradients (solid red) where neither of the distributions from GM nor WM is symmetric, the distributions of CV values in WM are closer to the normal distribution than those in GM.

Median and IQR values were used to quantitatively summarize the CV histograms given that they were not all normally distributed. **Table 1** shows the results for **Experiments 1** and **2** on four different subjects and **Table 2** for **Experiments 3** and **4** on one subject. These results indicate that the noise in

FIGURE 4 | CV maps (a,e) of the input images in **Experiments 3** and **4** (S_1 and S_2 respectively), **(b,f)** the experimentally obtained variability in the estimated T_1 maps using **Experimental variance evaluation**, and **(c,g)** the theoretically-predicted T_1 noise from the first term in Equation (5), i.e., $100 \cdot \sigma_{S_1} \cdot (\partial T_1 / \partial S_1) / \hat{T}_1$ and $100 \cdot \sigma_{S_2} \cdot (\partial T_1 / \partial S_2) / \hat{T}_1$ respectively (**Theoretical variance evaluation**). **(d)** The percentage difference between **(b)** and **(c)**. **(h)** The percentage difference between **(f)** and **(g)**. Results are shown separately for **Experiment 3 (a–d)** and **Experiment 4 (d–h)**. All CV maps shown were calculated by the equations shown in the corresponding gray boxes multiplied by 100. $\hat{S}_1$, $\hat{S}_2$, and $\hat{T}_1$ in gray boxes denote the average values of six S_1, S_2, and corresponding T_1 maps respectively.

S_1, S_2, and f_{B1} propagated similarly into the T_1 maps, such that the CV approximately doubled between the input signals and the calculated T_1 maps. Also, the CV values of the T_1 maps calculated via **Experimental** and **Theoretical variance evaluations** were similar in both GM and WM. As noted previously, the CV values decreased dramatically going from **Experiment 1** with small spoiler to **Experiment 2** with large spoiler. This was the case for subjects 1–3 (see **Table 1**). For subject 4, however, the CV values did not decrease (gray cell background in **Table 1**). This was likely due to instability in the RF transmit chain and it demonstrates the validity of the theoretical framework for different sources of error.

DISCUSSION

Using the VFA method, the precision of T_1 relaxation time measurements depends not only on the SNR of the SPGR images

but, crucially, also on the error propagated from the B_1^+ map that is used to correct the bias caused by spatial inhomogeneity in the achieved flip angle. The precision of the B_1^+ map is often overlooked as a source of uncertainty in T_1 measurements. Here we have derived analytical solutions for the error propagated to the T_1 relaxation time estimates (Equations 5–8). This analysis indicates that the three signal sources (the two SPGR images with different flip angles and the B_1^+ map) propagate noise into the T_1 estimates to approximately the same degree, with the CV approximately doubling between each of the three signal sources and the T_1 estimate (**Tables 1, 2**). By examining two distinct noise levels in the B_1^+ maps (by manipulating the degree of spoiling), we could show that the precision of the T_1 map can be greatly improved by increasing the precision of the B_1^+ mapping procedure.

We have experimentally validated the analytical framework by performing repeated experiments to estimate the voxel-wise

FIGURE 5 | The histograms of *CV* values for Experiments 1–4 inside GM (left) and WM (right). The solid lines, dashed lines, and circles represent the *CV* of the six input images, the experimental *CV* of T_1 calculated from the six input images (**Experimental variance evaluation**), and the theoretically-predicted *CV* of T_1 (**Theoretical variance evaluation**) respectively. The histograms for **Experiments 1–4** are shown with red, cyan, black and blue colors, respectively.

variance of the T_1 maps. We found overall agreement between the theoretical predictions ($\sigma_{T_1,\text{theo}}$) and the experimental measures ($\sigma_{T_1,\text{exp}}$), especially when the input noise, and accordingly T_1 noise, is small as in **Experiments 2** and **3**. For example, **Figure 4d** shows discrepancy of less than 1% inside GM and WM and relatively high discrepancy only in voxels containing cerebrospinal fluid (CSF), which we attribute to the fact that CSF has a significantly longer T_1 than GM and WM, for which the VFA sequence was optimized. With higher input noise the discrepancy between theory and measurement tended to increase (**Figures 3d**, **4h**). This is because Equation (5) predicts the propagated error correctly only when σ_{S_i} and $\sigma_{f_{B1}}$ are small enough that the constant slope approximation (i.e., constant partial derivative) is valid over the ranges of σ_{S_i} and $\sigma_{f_{B1}}$ in the S_i/f_{B1} vs. T_1 graph. Nonetheless, in the range of experimentally measured noise from our *in vivo* experiments, the discrepancies were small inside both GM and WM.

Subject 4 had high variability in f_{B1} and therefore in the estimated T_1, even in **Experiment 2**, which used big spoiler gradients to minimize the variance. This may be due to one of the parameters associated with the determination of the RF transmit voltage, which were observed to fluctuate more across the six B_1^+ acquisitions in subject 4 than across the acquisitions from the other three subjects. This fluctuation might be due to hardware instability in the RF transmit chain. The necessity to keep the RF transmit voltage constant for reliable quantification of T_1 has been reported previously in Lutti and Weiskopf (2013). Therefore, it is reasonable to consider the RF transmit instability as a reason behind the reduced precision of the repeated B_1^+ map acquisitions in this case. This observation demonstrates that not only the acquisition method, e.g., degree of spoiling used, but also

the hardware settings need to be considered when optimizing the precision of B_1^+, and by extension T_1, measurements.

The *CV* maps from **Experiment 1** had asymmetric left-right distributions as shown in **Figures 3a–c** for subject 1. While three out of four subjects manifested asymmetric distributions, one of them showed a strong pattern of left-right symmetry (data not shown), indicating that the spatial distribution of precision is subject-specific. This may be due to susceptibility effects from the air-tissue interface, how well the shimming procedure can correct for local field distortions, positioning of the subject in the scanner and interaction with the transmit field. We also found that the histograms of *CV* values in GM did not tend to be normally distributed compared to those in WM. This may be due to the fact that more GM voxels suffer partial volume effects with CSF and the VFA acquisition was optimized for the T_1 values of GM/WM not the significantly longer T_1 of CSF. The non-normal distributions in the histograms from **Experiment 1** for both GM and WM show that the B_1^+ maps with small spoiler gradients are dominated by noise sources other than thermal noise.

Because the transmit RF field map is smoothly varying, a commonly recommended practice for reducing noise in B_1^+ maps is spatial smoothing. It must be noted however that systematic offset in a given image cannot be corrected by spatial smoothing. As an example see **Figure 6** where the 6 B_1^+ maps from **Experiment 1** were smoothed by a 3D Gaussian kernel with standard deviation of $4 \times 4 \times 4$ mm^3. It is evident from the profile extracted from the white line in **Figure 6a** that spatial smoothing of the 6 individual B_1^+ maps separately leaves a systematic offset uncorrected (**Figures 6c,d**). In such cases, when thermal noise does not dominate the error sources but the systematic offset is random in the different repetitions, a more appropriate procedure is averaging multiple acquisitions. Although, repeated

TABLE 1 | Median and (IQR) of *CV* values inside GM and WM for Experiments 1–2.

		Experiment 1 (six B_1^+ w/small spoiler)		Experiment 2 (six B_1^+ w/big spoiler)	
		GM	WM	GM	WM
Subject 1	*CV* of repeated B_1^+ measurements	2.46 (1.99)	1.95 (1.23)	0.75 (0.44)	0.64 (0.37)
	Experimental *CV* of T_1	4.93 (4.04)	3.92 (2.52)	1.49 (0.88)	1.28 (0.73)
	Theoretical *CV* of T_1	4.90 (3.96)	3.89 (2.46)	1.49 (0.88)	1.28 (0.73)
Subject 2	*CV* of repeated B_1^+ measurements	2.67 (1.72)	1.77 (1.13)	0.70 (0.37)	0.59 (0.29)
	Experimental *CV* of T_1	5.37 (3.41)	3.54 (2.29)	1.39 (0.74)	1.19 (0.58)
	Theoretical *CV* of T_1	5.34 (3.43)	3.53 (2.26)	1.39 (0.74)	1.19 (0.58)
Subject 3	*CV* of repeated B_1^+ measurements	3.70 (2.18)	2.74 (1.32)	0.79 (0.42)	0.64 (0.35)
	Experimental *CV* of T_1	7.48 (4.62)	5.44 (2.71)	1.57 (0.84)	1.28 (0.69)
	Theoretical *CV* of T_1	7.38 (4.30)	5.46 (2.63)	1.57 (0.84)	1.28 (0.69)
Subject 4	*CV* of repeated B_1^+ measurements	2.91 (1.52)	2.11 (1.00)	3.30 (0.59)	3.28 (0.47)
	Experimental *CV* of T_1	5.81 (3.04)	4.21 (1.97)	6.77 (1.25)	6.75 (1.00)
	Theoretical *CV* of T_1	5.82 (3.03)	4.22 (1.98)	6.57 (1.17)	6.54 (0.93)

IQR, interquartile range; CV, coefficient of variation; GM, gray matter; WM, white matter.
Subject 4 had high variability in f_{B1} and T_1 (gray shade values) even in Experiment 2, which may be due to hardware instability in the RF transmit chain.

TABLE 2 | Median and IQR of *CV* values inside GM and WM for Experiments 3–4.

		Experiment 3 (six S1)		Experiment 4 (six S2)	
		GM	WM	GM	WM
Subject 1	*CV* of repeated S_1 or S_2 measurements	2.41 (1.17)	2.12 (0.92)	3.56 (1.83)	2.61 (1.03)
	Experimental *CV* of T_1	4.56 (2.23)	3.98 (1.73)	6.69 (3.58)	4.90 (1.94)
	Theoretical *CV* of T_1	4.55 (2.23)	3.98 (1.73)	6.69 (3.49)	4.90 (1.92)

IQR, interquartile range; CV, coefficient of variation; GM, gray matter; WM, white matter.

measurement of the B_1^+ map requires additional time, it is usually still the more efficient way to proceed because high-resolution SPGR images take significantly longer to acquire (in our case more than twice as long). This recommendation is further supported by our finding that the B_1^+ maps propagate approximately the same error as either of the two SPGR images.

When optimizing T_1 mapping protocols, previous work has focused mainly on optimizing acquisition parameter settings, most notably the flip angles used to acquire the SPGR images, that minimize uncertainty in the measured T_1 value (Weiss et al.,

1980; Wang et al., 1987; Schabel and Morrell, 2009; Helms et al., 2011; Wood, 2015). Although bias resulting from the spatial non-uniformity of the transmit RF transmit field is also well known and is commonly corrected by incorporating a B_1^+ map into the calculations (Helms et al., 2008; Yarnykh, 2010; Lutti et al., 2013; Stikov et al., 2015), the precision with which the B_1^+ map is obtained is typically ignored. Pohmann and Scheffler compared the precision of several B_1^+ mapping methods and found widely varying results depending on the method used and the nominal flip angle to be measured (Pohmann and Scheffler,

FIGURE 6 | Spatial smoothing effects in Experiment 1 with small spoiler gradients. (a) CV map of the six f_{B1} after smoothing. **(b)** CV map of the six T_1 maps estimated with the six smoothed f_{B1} (**Experimental variance evaluation**). **(c,d)** Profiles along the white line in **(a)** for the six original f_{B1} maps and six smoothed f_{B1} maps respectively.
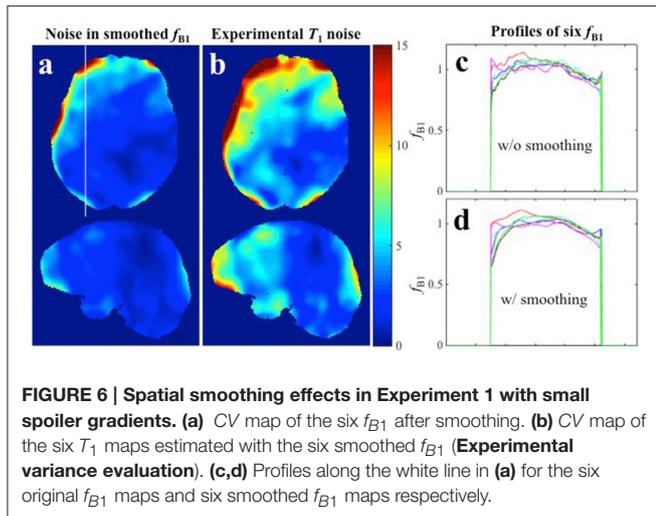
2013). Our results further demonstrate the necessity to consider the precision of B_1^+ mapping when using these to correct bias in the T_1 relaxation time maps. Rather than the assumed high precision estimate of T_1 (**Figure 1A**), one may arrive at a result that on the average is correct but may also have a high level of uncertainty (**Figure 1B**). This will have the greatest impact *in vivo* where there are more sources of noise (e.g., physiologically driven noise) and will reduce the detectable effect size in both cross-sectional and longitudinal studies in which T_1 measurements are used as a biomarker (Lutti et al., 2013).

In this study we used the AFI method for B_1^+ mapping, which was proposed and optimized by Yarnykh (Yarnykh, 2007, 2010) and has been shown to perform comparatively well (Pohmann and Scheffler, 2013). From **Experiments 1–2**, we showed that increasing spoiler gradients makes the estimation of T_1 not only more accurate as previously reported (Yarnykh, 2010) but also more precise due to the complete spoiling of the transverse magnetization. Pohmann and Scheffler (2013) found that for a 60° nominal flip angle their implementation of the AFI method had an uncertainty of 3° (5%) in simulations and 4° (7.5%) in phantom experiments. The CV of approximately 3% in the B_1^+ map that we observed *in vivo* (**Tables 1, 2**) is in line with these findings, and may even underestimate the B_1^+ related variance that can be expected to propagate into common T_1 mapping protocols from the map. However, the theoretical framework presented here makes no assumption on the choice of B_1^+ mapping approach. These findings are equally applicable, regardless of the B_1^+ mapping method used or how it was optimized to have high precision.

In both the *in vivo* experimental variance (**Experimental variance evaluation**) and the theoretical framework (**Theoretical variance evaluation**) we considered the noise propagating from the three input signals separately (Equations 5–8 and **Experiments 1–4**). This provides a convenient way in which to compare the effect of the three noise sources on the uncertainty of the final T_1 map. In practice, however, the errors propagating from the three sources are summed (Equation 5). Although CVs for the averaged SPGR signals and the B_1^+ maps were

similar in our *in vivo* experiments, the precision of B_1^+ maps can vary significantly depending on the B_1^+ mapping approach (see for example **Figure 6** in Pohmann and Scheffler, 2013), which shows that in phantom measurements some of the B_1^+ mapping methods, especially the 2D variants, can suffer higher uncertainty for certain acquisition parameter sets). Therefore, neglecting the uncertainty in the B_1^+ map can lead to significant erroneous overestimation of the precision of the calculated T_1 value.

Also note that including more than two SPGR images with more than two different flip angles for the T_1 estimation may even lead to the increased variability in T_1 since the noise from the additional SPGR images is additive to the total variance in T_1 ($\sigma_{T_1}^2$) according to Equation (5). This is also reflected by the fact that previous evaluations of uncertainty within the VFA regime conclude that when acquiring additional images the optimal approach is to acquire at the same flip angle and average (Wang et al., 1987; Helms et al., 2011).

To assess the uncertainty in the measurements of SPGR images and B_1^+ maps we performed repeated *in vivo* experiments for each of the input images. In such an approach, the uncertainty in each variable includes all sources, e.g., thermal noise, scanner instability, scanner drift, physiological noise and the test/re-test variability (e.g., differences in the optimized shim currents, or power amplifier calibration etc.), whereas usually only the thermal noise components are considered (Cheng and Wright, 2006). Had we simply estimated the thermal noise component by extracting the standard deviation of pixels in the background the theoretically-predicted uncertainty (**Theoretical variance evaluation**) would have seriously underestimated the uncertainty found in the *in vivo* T_1 relaxation time measurement (**Experimental variance evaluation**). In addition we would have confounds due to the Rician noise distribution of magnitude images and the image reconstruction scheme chosen (Constantinides et al., 1997).

A wide array of methods exists for measuring the T_1 relaxation time (Kingsley, 1999). A recently proposed method (Helms et al., 2008) was chosen here because it has been broadly used (Dick et al., 2012; Sereno et al., 2013; Callaghan et al., 2014) and optimized (Helms et al., 2011). However, our findings regarding the dependence of the precision of the T_1 measurement on the level of uncertainty in the B_1^+ map is not expected to be unique to this method of T_1 relaxation time measurement.

We conclude that when estimating the uncertainty of T_1 mapping methods, the error propagated from the B_1^+ map must also be considered. Optimizing the SPGR signals while neglecting to improve the precision of the B_1^+ map will result in a significant underestimation of the final uncertainty in the calculated T_1 relaxation time. Maximizing the precision of the adopted B_1^+ mapping approach is crucial for studies using T_1 as an imaging biomarker, which require high sensitivity (minimum variance), e.g., to investigate subtle differences in the micro-architectural organization of the brain.

ETHICS STATEMENT

This study was carried out in accordance with the recommendations of The Kantonale Ethics Komitee

(i.e., regional ethics committee) of Zurich with written informed consent from all subjects. The protocol was approved by The Kantonale Ethics Komitee.

AUTHOR CONTRIBUTIONS

YL, MC, and ZN designed the study; YL and ZN acquired the data; MC provided software for data analysis; YL, MC, and ZN analyzed data, interpreted the results and wrote the manuscript.

REFERENCES

Bevington, P. R., and Robinson, D. K. (2003). *Data Reduction and Error Analysis for the Physical Sciences.* Boston, MA: McGraw-Hill.

Callaghan, M. F., Freund, P., Draganski, B., Anderson, E., Cappelletti, M., Chowdhury, R., et al. (2014). Widespread age-related differences in the human brain microstructure revealed by quantitative magnetic resonance imaging. *Neurobiol. Aging.* 35, 1862–1872. doi: 10.1016/j.neurobiolaging.2014.02.008

Cheng, H. L., and Wright, G. A. (2006). Rapid high-resolution T(1) mapping by variable flip angles: accurate and precise measurements in the presence of radiofrequency field inhomogeneity. *Magn. Reson. Med.* 55, 566–574. doi: 10.1002/mrm.20791

Christensen, K. A., Grant, D. M., Schulman, E. M., and Walling, C. (1974). Optimal determination of relaxation times of fourier transform nuclear magnetic resonance. Determination of spin-lattice relaxation times in chemically polarized species. *J. Phys. Chem.* 78, 1971–1977. doi: 10.1021/j100612a022

Constantinides, C. D., Atalar, E., and McVeigh, E. R. (1997). Signal-to-noise measurements in magnitude images from NMR phased arrays. *Magn. Reson. Med.* 38, 852–857. doi: 10.1002/mrm.1910380524

Cunningham, C. H., Pauly, J. M., and Nayak, K. S. (2006). Saturated double-angle method for rapid B1+ mapping. *Magn. Reson. Med.* 55, 1326–1333. doi: 10.1002/mrm.20896

Deoni, S. C. (2007). High-resolution T1 mapping of the brain at 3T with driven equilibrium single pulse observation of T1 with high-speed incorporation of RF field inhomogeneities (DESPOT1-HIFI). *J. Magn. Reson. Imaging* 26, 1106–1111. doi: 10.1002/jmri.21130

Deoni, S. C., Peters, T. M., and Rutt, B. K. (2004). Determination of optimal angles for variable nutation proton magnetic spin-lattice, T1, and spin-spin, T2, relaxation times measurement. *Magn. Reson. Med.* 51, 194–199. doi: 10.1002/mrm.10661

Deoni, S. C., Peters, T. M., and Rutt, B. K. (2005). High-resolution T1 and T2 mapping of the brain in a clinically acceptable time with DESPOT1 and DESPOT2. *Magn. Reson. Med.* 53, 237–241. doi: 10.1002/mrm.20314

Dick, F., Tierney, A. T., Lutti, A., Josephs, O., Sereno, M. I., and Weiskopf, N. (2012). *In vivo* functional and myeloarchitectonic mapping of human primary auditory areas. *J. Neurosci.* 32, 16095–16105. doi: 10.1523/JNEUROSCI.1712-12.2012

Dowell, N. G., and Tofts, P. S. (2007). Fast, accurate, and precise mapping of the RF field *in vivo* using the 180 degrees signal null. *Magn. Reson. Med.* 58, 622–630. doi: 10.1002/mrm.21368

Drain, L. E. (1949). A direct method of measuring nuclear spin-lattice relaxation times. *Pro. Phys. Soc. Sect. A.* 62:301. doi: 10.1088/0370-1298/62/5/306

Fram, E. K., Herfkens, R. J., Johnson, G. A., Glover, G. H., Karis, J. P., Shimakawa, A., et al. (1987). Rapid calculation of T1 using variable flip angle gradient refocused imaging. *Magn. Reson. Imaging* 5, 201–208. doi: 10.1016/0730-725X(87)90021-X

Ganter, C. (2006). Steady state of gradient echo sequences with radiofrequency phase cycling: analytical solution, contrast enhancement with partial spoiling. *Magn. Reson. Med.* 55, 98–107. doi: 10.1002/mrm.20736

Haase, A., Frahm, J., Matthaei, D., Hanicke, W., and Merboldt, K. D. (1986). FLASH imaging. Rapid NMR imaging using low flip-angle pulses. *J. Magn. Reson.* 67, 258–266. doi: 10.1016/0022-2364(86)90433-6

Hahn, E. L. (1949). An accurate nuclear magnetic resonance method for measuring spin-lattice relaxation times. *Phys. Rev.* 76:145. doi: 10.1103/PhysRev.76.145

Harkins, K. D., Xu, J., Dula, A. N., Li, K., Valentine, W. M., Gochberg, D. F., et al. (2016). The microstructural correlates of T1 in white matter. *Magn. Reson. Med.* 75, 1341–1345. doi: 10.1002/mrm.25709

Helms, G., Dathe, H., and Dechent, P. (2008). Quantitative FLASH MRI at 3T using a rational approximation of the ernst equation. *Magn. Reson. Med.* 59, 667–672. doi: 10.1002/mrm.21542

Helms, G., Dathe, H., Weiskopf, N., and Dechent, P. (2011). Identification of signal bias in the variable flip angle method by linear display of the algebraic ernst equation. *Magn. Reson. Med.* 66, 669–677. doi: 10.1002/mrm.22849

Insko, E. K., and Bolinger, L. (1993). Mapping of the radiofrequency field. *J. Magn. Reson. Ser. A* 103, 82–85. doi: 10.1006/jmra.1993.1133

Jiru, F., and Klose, U. (2006). Fast 3D radiofrequency field mapping using echo-planar imaging. *Magn. Reson. Med.* 56, 1375–1379. doi: 10.1002/mrm.21083

Kingsley, P. B. (1999). Methods of measuring spin-lattice (T1) relaxation times: an annotated bibliography. *Concepts. Magn. Reson.* 11, 243–276. doi: 10.1002/(SICI)1099-0534(1999)11:4<243::AID-CMR5>3.0.CO;2-C

Liberman, G., Louzoun, Y., and Ben Bashat, D. (2014). T1 mapping using variable flip angle SPGR data with flip angle correction. *J. Magn. Reson. Imaging* 40, 171–180. doi: 10.1002/jmri.24373

Lutti, A., Dick, F., Sereno, M. I., and Weiskopf, N. (2013). Using high-resolution quantitative mapping of R1 as an index of cortical myelination. *Neuroimage* 93, 176–188. doi: 10.1016/j.neuroimage.2013.06.005

Lutti, A., Hutton, C., Finsterbusch, J., Helms, G., and Weiskopf, N. (2010). Optimization and validation of methods for mapping of the radiofrequency transmit field at 3T. *Magn. Reson. Med.* 64, 229–238. doi: 10.1002/mrm.22421

Lutti, A., and Weiskopf, N. (2013). "Optimizing the accuracy of T1 mapping accounting for RF non-linearities and spoiling characteristics in FLASH imaging," in *Proceedings of the 21st Annual Meeting of ISMRM.* (Utah, UT).

Nehrke, K., and Börnert, P. (2012). DREAM - A novel approach for robust, ultrafast, multislice B1 mapping. *Magn. Reson. Med.* 68, 1517–1526. doi: 10.1002/mrm.24158

Pohmann, R., and Scheffler, K. (2013). A theoretical and experimental comparison of different techniques for B1 mapping at very high fields. *NMR Biomed.* 26, 265–275. doi: 10.1002/nbm.2844

Preibisch, C., and Deichmann, R. (2009). Influence of RF spoiling on the stability and accuracy of T1 mapping based on spoiled FLASH with varying flip angles. *Magn. Reson. Med.* 61, 125–135. doi: 10.1002/mrm.21776

Pruessmann, K. P., Weiger, M., Scheidegger, M. B., and Boesiger, P. (1999). SENSE: sensitivity encoding for fast MRI. *Magn. Reson. Med.* 42, 952–962. doi: 10.1002/(SICI)1522-2594(199911)42:5<952::AID-MRM16>3.0.CO;2-S

Sacolick, L. I., Wiesinger, F., Hancu, I., and Vogel, M. W. (2010). B1 mapping by bloch-siegert shift. *Magn. Reson. Med.* 63, 1315–1322. doi: 10.1002/mrm.22357

Schabel, M. C., and Morrell, G. R. (2009). Uncertainty in T1 mapping using the variable flip angle method with two flip angles. *Phys. Med. Biol.* 54:N01. doi: 10.1088/0031-9155/54/1/N01

Sereno, M. I., Lutti, A., Weiskopf, N., and Dick, F. (2013). Mapping the human cortical surface by combining quantitative T(1) with retinotopy. *Cereb. Cortex.* 23, 2261–2268. doi: 10.1093/cercor/bhs213

Stikov, N., Boudreau, M., Levesque, I. R., Tardif, C. L., Barral, J. K., and Pike, G. B. (2015). On the accuracy of T1 mapping: searching for common ground. *Magn. Reson. Med.* 73, 514–522. doi: 10.1002/mrm.25135

Venkatesan, R., Lin, W., and Haacke, E. M. (1998). Accurate determination of spin-density and T1 in the presence of rf-field inhomogeneities and flip-angle miscalibration. *Magn. Reson. Med.* 40, 592–602. doi: 10.1002/mrm.1910400412

Wang, H. Z., Riederer, S. J., and Lee, J. N. (1987). Optimizing the precision in T1 relaxation estimation using limited flip angles. *Magn. Reson. Med.* 5, 399–416. doi: 10.1002/mrm.1910050502

Weiss, G. H., Guptaj, R. K., Ferretti, J. A., and Becker, E. D. (1980). The choice of optimal parameters for measurement of spin-lattice relaxation times. I. Mathematical formulation. *J. Magn. Reson.* 37, 369–379. doi: 10.1016/0022-2364(80)90044-x

Wood, T. C. (2015). Improved formulas for the two optimum VFA flip-angles. *Magn. Reson. Med.* 74, 1–3. doi: 10.1002/mrm.25592

Yarnykh, V. L. (2007). Actual flip-angle imaging in the pulsed steady state: a method for rapid three-dimensional mapping of the transmitted radiofrequency field. *Magn. Reson. Med.* 57, 192–200. doi: 10.1002/mrm.21120

Yarnykh, V. L. (2010). Optimal radiofrequency and gradient spoiling for improved accuracy of T1 and B1 measurements using fast steady-state techniques. *Magn. Reson. Med.* 63, 1610–1626. doi: 10.1002/mrm.22394

Zur, Y., Wood, M. L., and Neuringer, L. J. (1991). Spoiling of transverse magnetization in steady-state sequences. *Magn. Reson. Med.* 21, 251–263. doi: 10.1002/mrm.1910210210